Model-Based Analysis of a Gas/Vapor–Liquid Microchannel Membrane Contactor

Anna Lautenschleger
Chair of Fluid Process Engineering, Faculty of Mechanical Engineering, University of Paderborn, Pohlweg 55, D-33098 Paderborn, Germany

Eugeny Y. Kenig
Chair of Fluid Process Engineering, Faculty of Mechanical Engineering, University of Paderborn, Pohlweg 55, D-33098 Paderborn, Germany

Gubkin Russian State University of Oil and Gas, Leninsky Prospect 65, 119991 Moscow, Russian Federation

Andreas Voigt and Kai Sundmacher
Otto-von-Guericke-University Magdeburg, Process Systems Engineering, Universitätsplatz 2, D-39106 Magdeburg, Germany

Max-Planck Institute for Dynamics of Complex Technical Systems, Sandtorstrasse 1, D-39106 Magdeburg, Germany

DOI 10.1002/aic.14784
Published online March 30, 2015 in Wiley Online Library (wileyonlinelibrary.com)

A comprehensive numerical investigation on membrane distillation of methanol and water in a microseparator was carried out. The focus was to investigate the impact of the apparatus geometry on the separation performance and to develop alternative designs for process intensification. To describe the process, a computational fluid dynamics-based model was developed and validated against experimental data from literature. Based on this model, parametric studies were performed to gain a deeper understanding of the microchannel geometry influence. Furthermore, two geometry modifications were suggested and analyzed, a miniaturization of the channel and an implementation of baffles. The modification with baffles was chosen for a new separator design which was studied experimentally, and the obtained experimental data were used for another model validation, this time for the baffle arrangement. Subsequent comprehensive simulations were performed to investigate mass-transfer enhancement by the modified geometry. Generally, the baffles reveal a considerable potential for the process intensification. © 2015 American Institute of Chemical Engineers *AIChE J*, 61: 2240–2256, 2015

Keywords: computational fluid dynamics, design, distillation, membrane, separations, microfluidics

Introduction

Microseparation processes represent an essential way toward process intensification. In the past decades, innovative microstructured units were developed allowing different separation processes at microscale to be realized. Examples are absorption/desorption,[1–3] extraction,[4–6] and distillation.[7–13] However, despite significant progress, the microseparation technology is still far from being established as mature technology, as the technical barriers resulting from the miniaturization are difficult to overcome. This especially refers to the conventional distillation process at microscale. Due to the fact that, at this scale, surface forces dominate over body forces, the evaporation behavior is hard to control, in particular under countercurrent flow conditions. Nevertheless, several research groups have been actively working on different methods to establish a stable vapor–liquid flow in microdistillation units. For instance, capillary forces were used to replace gravity as the liquid-phase driving force. This principle was first introduced in 1985 by Seok and Hwang.[7] They used a horizontal pipe with walls covered by fiberglass within which the liquid phase moved. Due to the heating of one end of the tube and cooling of the other end, capillary forces were induced in the wetted fiberglass resulting in the liquid-phase movement. The gas phase flowed countercurrently along the tube. This separation process was called "zero-gravity distillation." Tschernjaew et al.[14] developed a mathematical model to describe the separation of a multicomponent mixture in the zero-gravity distillation column. The simulation results confirmed the high performance of this separation unit. Sundberg et al.[10] designed a similar distillation column. The horizontally oriented device was flat, and on its bottom, a metal foam was placed instead of the fiberglass. Furthermore, Lam et al.[11,12] developed microscale distillation chips with different channel configurations. One side of the channels was covered by micropillars to

Correspondence concerning this article should be addressed to E. Y. Kenig at eugeny.Kenig@upb.de.

conduct the liquid phase by capillary forces in counterflow to the gas phase. In all these works, a high-separation efficiency was reported yet at a very low-feed rate.

Instead of capillary forces, MacInnes et al.[13] applied a centrifugal force to transport the liquid phase. A prototype device containing a rotating spiral microchannel was designed and used in an experimental study. This construction, however, requires a high technical effort to generate the centrifugal force.

An alternative approach is the use of a permeable membrane by which the gas–liquid interface is stabilized and which allows for dispersionless contact of the two phases. The wetting property of the membrane ensures that either the polar or the unpolar phase is prevented from crossing the membrane and penetrating into the other phase. The flow of both gas and liquid phase is induced by the pressure gradient along the channel. This principle is used by the so-called sweep gas membrane distillation.[15] Here, the process takes place below the boiling point, and the separation is based on the difference in partial vapor pressures of the relevant species. Volatile species evaporate at the hot liquid/vapor interface, cross the membrane and are swept by the cold inert gas out of the separation zone. The separation here rather reminds a desorption process than convertional distillation. However, the term "membrane distillation" is common in the literature for the separation of volatile species from a liquid mixture with the help of a membrane, and in this work, we pursue the same course. In Ref. 15, a comprehensive overview of the different membrane distillation variants is given.

The membrane distillation was implemented in a microscale contactor by Adiche and Sundmacher.[16] Experimental investigations were carried out with this microseparator using the test mixture methanol/water at different operating conditions. In these experiments, the feasibility of the separation in the microchannel membrane distillation device was proven. Furthermore, it was shown that the process could be performed in a wide range of volumetric gas and liquid flow rates, as long as the liquid entry pressure of the membrane was not exceeded. This is due to the fact that the flows of both phases are separated by the membrane, and therefore, no shear stresses act between them. In this respect, the presented microseparator offers the potential for an intensified distillation process with a flexible operating range of the gas and liquid flow rates. However, further investigations are needed to optimise its performance with respect to mass transfer and pressure drop.

In this work, we present a novel and universal computational fluid dynamics (CFD)-based modeling approach to the membrane distillation process. It enables a detailed description of the transport phenomena inside arbitrary micromembrane distillation units and takes membrane characteristics into account. The approach provides a deeper understanding of the physical processes interacting in the micromembrane separator designed by Adiche and Sundmacher,[16] and it was validated using experimental data from Ref. 16. Along these lines, a thorough investigation of different apparatus geometries and, consequently, the development of alternative designs for process intensification becomes feasible. In this respect, two different aspects were investigated: (1) the effect of further miniaturization of the separation unit and (2) the use of baffles integrated in the fluid-phase channels. Both intensification approaches were evaluated with respect to mass-transfer and pressure drop characteristics.

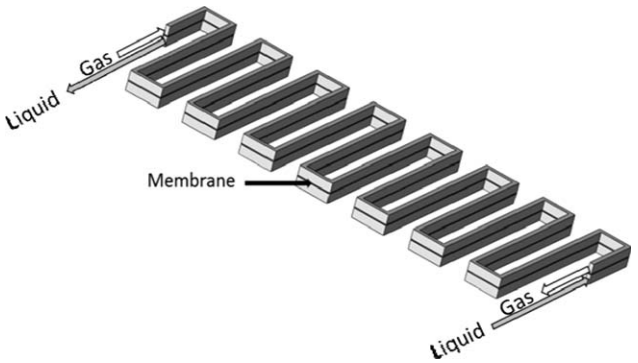

Figure 1. Micromembrane distillation unit consisting of two microchannels and a hydrophobic membrane between them.

Microseparator Geometry and Characteristics

The microseparator consists of two horizontal polycarbonate plates which are joined together holding a flat microporous hydrophobic membrane in between. In each plate, a meandering rectangular channel is milled, with the dimensions $342 \times 0.5 \times 1$ mm^3 (length $\times$ width $\times$ height). More details about the microseparator can be found in Ref. 16. Figure 1 shows how the liquid phase flows through one microchannel, whereas the carrier inert gas flows through the other microchannel, tangentially to the membrane surface and in countercurrent mode.

Three commercial types of flat sheet polymeric microporous membrane were used.[16] Their characteristics are summarized in Table 1.

Process Description

The experimental setup of the membrane distillation process is shown in Figure 2. It consists of the microseparator (1), the liquid feed line (2), a circulation pump (3), a microheat exchanger (4), a permeate trap (5) in the ice bath cooler (6) and with a nitrogen exhaust (7), a measuring cup for the retentate (8), and a nitrogen supply (9). More details about the experimental equipment are given in Ref. 16.

The feed consisting of methanol and water is heated by a microheat exchanger before entering the microseparator. The inert gas consisting of dry nitrogen is fed into the separator. As a hydrophobic membrane is used, the methanol/water mixture is repelled by the membrane surface, whereas the gas phase fills the membrane pores. At the entrance of the pores, a stable gas–liquid interface is established, where water and methanol evaporate according to their chemical potential and cross the membrane. The cold inert gas sweeps the permeate out of the separation unit. To determine the mass fluxes of methanol and water crossing the membrane, the gas phase is led into the ice bath cooler in which methanol and water condense. When the experiment is finished, the collected permeate is weighted. The resulting weight divided by the membrane effective area and the duration of experiment gives the total mass flux of the methanol/water mixture through the membrane. Furthermore, the methanol mass fraction of the permeate is determined by gas chromatography, and the separation factor is calculated as follows

$$S = \left(\frac{W_{\text{methanol,permeate}}}{1 - W_{\text{methanol,permeate}}}\right) \cdot \left(\frac{1 - W_{\text{methanol,feed}}}{W_{\text{methanol,feed}}}\right) \qquad (1)$$

Table 1. Characteristics of the Tested Microporous Membranes[16]

Membrane	Pore Size (μm)	Thickness (μm)	Porosity (vol. %)]	Entry Pressure of Water (bar)
PES40: oleophobic polyether-sulfone polymer cast on a nonwoven polyester support membrane by Pall (USA)	0.40	166	0.55	1.37
PVDF22: hydrophobic poly-vinylidene fluoride membrane by Millipore (USA)	0.22	114	0.75	2
ePTFE45: oleophobic expanded polytetrafluoroethylene membrane on a nonwoven polyester support by Gore (USA)	0.45	250	0.91	1.3

Modeling

To describe the process of the membrane distillation in the microseparator, a mathematical model was developed which included the liquid-phase and gas-phase fluid dynamics as well as the coupled heat and mass transfer in the channels and through the membrane. Figure 3a gives a schematic representation of the energy and mass transport through a membrane pore. For the calculation of the fluxes through the membrane, we assumed an average porosity, pore size, and tortuosity and neglected the phase interface curvature at the entrance of the membrane pore openings.

The geometry shown in Figure 1 was used as a basis for the three-dimensional (3-D) model domain. Figure 3b illustrates a 2-D view of this domain with the corresponding boundaries visualized by dashed arrows. Boundary A is the wall, boundary B is the inlet, and boundary C is the outlet. At boundary D, the no-slip condition for the momentum balance equation and the flux continuity for the energy and mass balance equations are valid.

Energy and mass transport are treated separately from the momentum transport. First, the velocity field in the microchannels is considered and determined. Afterwards, the temperature and concentration fields are calculated based on the velocity field. This approach is justified, as the change of the temperature and concentration is relatively small, and thus, it has hardly any impact on the flow field.

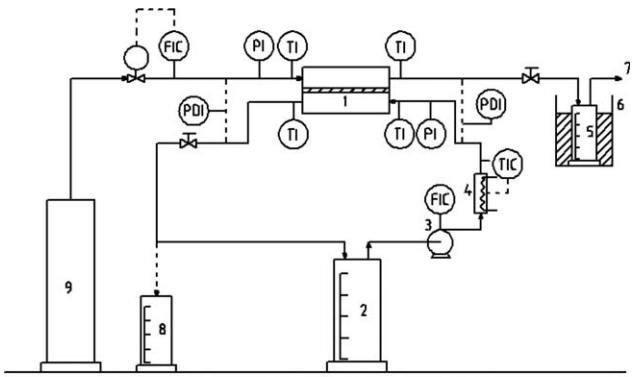

1	Micro-separator	6	Cooler(water-ice bath)
2	Liquid Feed	7	Nitrogen exhaust
3	Circulating pump	8	Retentate
4	Micro heat exchanger	9	Nitrogen supply
5	Permeate		

Figure 2. Experimental setup; PDI: measured pressure difference, PI: measured pressure, TI: measured temperature, TIC: controlled temperature, FIC: controlled flow rate[16].

To compare the total mass flux through the membrane and the separation factor resulting from the simulation with the corresponding experimental values, the condensation process taking place in the ice bath cooler installed after the microseparator was also taken into account. This process was considered as a single equilibrium stage at a temperature of $T = 0°C$ and ambient pressure. The equilibrium calculation was performed using Aspen Plus®.

Flow field

The flow of each phase is described by means of the continuity and steady-state Navier–Stokes equations

$$\nabla \cdot \vec{u} = 0 \tag{2}$$

$$\nabla \cdot \rho \vec{u}\vec{u} = -\nabla p + \rho \vec{g} + \eta \Delta \vec{u} \tag{3}$$

where $\vec{u}$ is velocity vector, $\vec{g}$ is gravity, p is pressure, ρ is density, and η is dynamic viscosity.

The no-slip boundary condition was applied to all walls of the microchannel including the surface of the membrane (dashed arrows A and D in Figure 3b). At the inlet of the microchannels (B in Figure 3b), the velocity value was preset while at their outlet, the pressure was set equal to atmospheric pressure (C in Figure 3b)

$$\vec{u}_{\text{wall}} = 0 \tag{4}$$

$$\vec{u}_{\text{inlet}} = \vec{u_0} \tag{5}$$

$$p_{\text{outlet}} = p_{\text{atm}} \tag{6}$$

Energy transport

The energy transfer in the gas and liquid phase is governed by the following equation

$$\rho c_{\text{p}} \vec{u} \cdot \nabla T = \nabla(\lambda \nabla T) \tag{7}$$

where T stands for temperature, c_{p} for the specific heat capacity, and λ for thermal conductivity. The velocity vector $\vec{u}$ represents an external variable determined from Eqs. 2–6.

At the inlet boundaries (B in Figure 3b), temperature values were preset and the walls were assumed to be thermally isolated (A in Figure 3b). At the outlet boundaries, the conductive heat flux was neglected being small compared to the respective convective flux (C in Figure 3b)

$$T_{\text{inlet}} = T_0 \tag{8}$$

$$q_{\text{wall}} = \vec{n} \cdot (-\lambda \nabla T + \vec{u} T) = 0 \tag{9}$$

$$q_{\text{out}} = \vec{n} \cdot (-\lambda \nabla T) = 0 \tag{10}$$

When calculating the heat flux through the membrane represented by D in Figure 3b, uniform pore distribution along

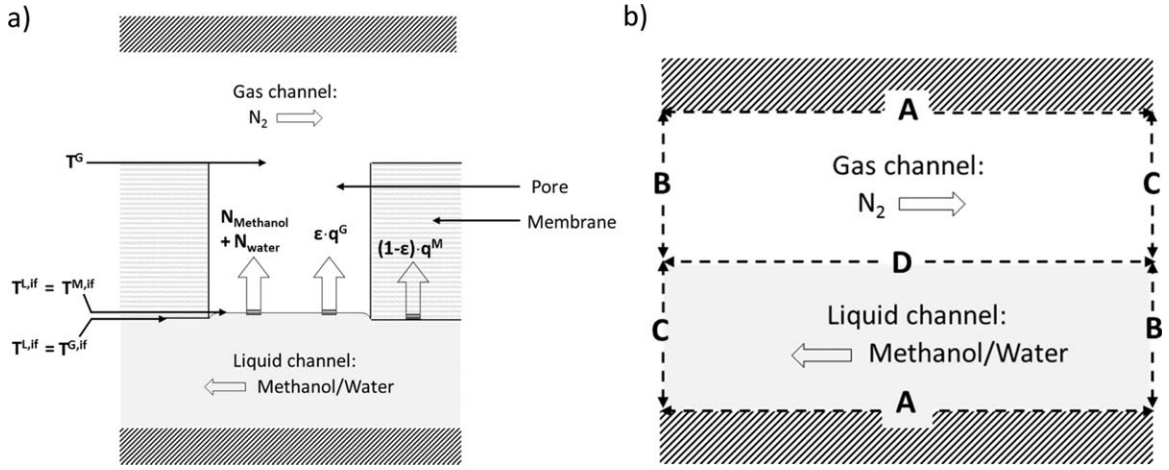

Figure 3. Schematic view of the energy and mass transport through a membrane pore (a); 2-D view of the model domain with the corresponding boundaries (b).

the membrane was assumed. The contact angle of the aqueous phase on the membranes under study lies between 100° and 120°.[17,18] As a consequence of the hydrophobic coating of the pores, they were considered to be completely filled with gas. At the lower surface of the membrane, the heat is transferred from the liquid to the gas phase located in membrane pores as well as to the membrane material. As shown in Figure 3a, at the gas–liquid interface, the temperature of the liquid phase was assumed to be equal to that of the gas phase while at the membrane-liquid interface, the temperature of the membrane was assumed to be equal to that of liquid phase

$$T^{\mathrm{L,if}} = T^{\mathrm{M,if}} \quad \text{and} \quad T^{\mathrm{L,if}} = T^{\mathrm{G,if}} \tag{11}$$

where $T^{\mathrm{L,if}}$ is the temperature of the liquid phase, $T^{\mathrm{M,if}}$ is the temperature of membrane material, and $T^{\mathrm{G,if}}$ is the temperature of the gas phase at the gas–liquid interface. In our model, the increase of the interface area due to the curvature visible in Figure 3a was neglected. This is justified, as the pressure in both phases is close to 1 bar. Furthermore, heat flux continuity should be fulfilled at the gas–liquid interface as well as at the membrane-liquid interface

$$q^{\mathrm{L,if}} = \vec{\mathrm{n}} \cdot (-\lambda^{\mathrm{L}} \nabla T^{\mathrm{L}}) = q^{\mathrm{G/M,if}} \tag{12}$$

$q^{\mathrm{G/M,if}}$ represents the heat transfer in the membrane comprising the heat conduction in the gas phase and in the membrane material as well as the evaporation of methanol and water

$$q^{\mathrm{G/M,if}} = \varepsilon\lambda^{\mathrm{G}}\left(\frac{T^{\mathrm{G,if}} - T^{\mathrm{G}}}{L_{\mathrm{membrane}}}\right) + (1-\varepsilon)\lambda^{\mathrm{M}}\left(\frac{T^{\mathrm{M,if}} - T^{\mathrm{G}}}{L_{\mathrm{membrane}}}\right) + \Delta H^{\mathrm{V}}_{\mathrm{methanol}} N^{\mathrm{if}}_{\mathrm{methanol}} + \Delta H^{\mathrm{V}}_{\mathrm{water}} N^{\mathrm{if}}_{\mathrm{water}} \tag{13}$$

where L_{membrane} is the thickness of the membrane and ε is membrane porosity.

Mass transport

The mass transport in the liquid phase (methanol/water mixture) is governed by the following differential methanol mass balance

$$\vec{\mathrm{u}} \cdot \nabla x_{\mathrm{methanol}} = \nabla(D^{L} \nabla x_{\mathrm{methanol}}) \tag{14}$$

where x is molar fraction and D is binary diffusion coefficient. The molar fraction of water can be obtained by means of the following summation condition

$$x_{\mathrm{methanol}} + x_{\mathrm{water}} = 1 \tag{15}$$

The mass transfer in the ternary gas-phase system (nitrogen/methanol/water) was described using the Maxwell–Stefan equations. The gas phase was considered to be an ideal fluid. In this case, the Maxwell–Stefan equations can be expressed in a 2 × 2 matrix form

$$\vec{\mathbf{J}} = -C^{\mathrm{G}}_{\mathrm{tot}} [\mathbf{B}]^{-1} \nabla \mathbf{y} \tag{16}$$

where $\mathbf{y}$ is the vector of component molar fractions and $[\mathbf{B}]$ is a quadratic matrix with the following elements[19]

$$\mathrm{B}_{ii} = \frac{y_i}{D^{\mathrm{SM}}_{i3}} + \sum_{\substack{k=1 \\ i \neq k}}^{3} \frac{y_k}{D^{\mathrm{SM}}_{ik}} \tag{17}$$

$$\mathrm{B}_{ij} = -y_i \left(\frac{1}{D^{\mathrm{SM}}_{ij}} - \frac{1}{D^{\mathrm{SM}}_{i3}}\right) \quad (i \neq j) \tag{18}$$

where y_i is molar fraction of ith component in the gas phase and D^{SM}_{ij} is binary Maxwell–Stefan diffusion coefficient of the components i and j. The mass-transfer equation for a multicomponent system is expressed as follows

$$\vec{\mathrm{u}} \cdot \nabla \mathbf{y} = \nabla\left([\mathbf{B}]^{-1} \nabla \mathbf{y}\right) \tag{19}$$

where $\vec{\mathrm{u}}$ is velocity vector determined by Eqs. 2–6. The elements of the square matrix $[\mathbf{B}]$ can be obtained based on the binary Stefan–Maxwell diffusion coefficients.

For the mass transport through the membrane, a uniform pore distribution across the membrane was assumed, similar as for the energy transport. Figure 3a illustrates the transport of methanol and water through a single membrane pore. As the radius of the pore is significantly larger than the molecular mean free path length of the species methanol and water in the gas phase, Knudsen diffusion can be excluded. The membrane material itself is impermeable for the species. At the gas–liquid interface of each pore, thermodynamic equilibrium and the component flux continuity for methanol and water have to be fulfilled

$$y_i = \frac{p^0_i}{p_{\mathrm{tot}}} \cdot \gamma_i \cdot x_i \tag{20}$$

$$N^{L,\mathrm{if}}_i = \vec{\mathrm{n}} \cdot \left(-C^{L}_{\mathrm{tot}} D^{L} \nabla x_i\right) = N^{\mathrm{G,if}}_i \tag{21}$$

where p^0_i is saturation vapor pressure of the pure component, and γ is activity coefficient. p_{tot} is total pressure in the gas channel resulting from Eqs. 2–6.

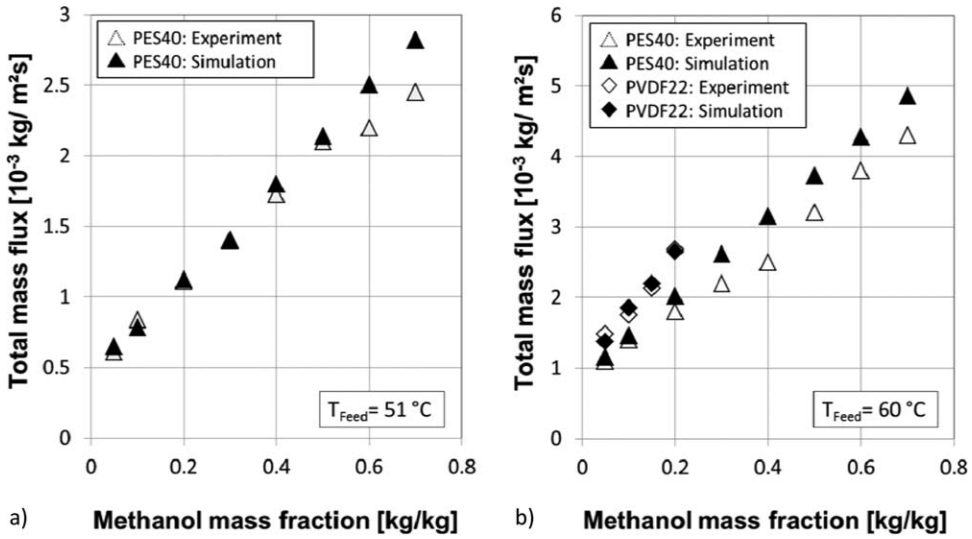

Figure 4. Comparison of the simulated and measured mass fluxes of the methanol/water mixture through the membrane for different feed compositions and the inlet temperatures of 51°C (a) and 60°C (b) for the membrane of type PES40 and PVDF22.

To determine the mass fluxes of methanol and water $N_i^{\mathrm{G,if}}$ through the membrane pore, we assumed a stagnant gas phase inside it. The evaporated methanol and water diffuse from the liquid surface through the pore. In contrast, the liquid surface is considered impermeable to nitrogen. As no accumulation of the considered species in the pore occurs, the mass fluxes are constant throughout the membrane pore. The flux of nitrogen at the interface is zero, which implies that it is zero everywhere in the membrane pore. Due to this fact, the total flux through the pore consists solely of methanol and water, and the species mass fluxes are given as

$$N_{\mathrm{methanol}}^{\mathrm{G,if}} = y_{\mathrm{methanol}}\left(N_{\mathrm{methanol}}^{\mathrm{G,if}} + N_{\mathrm{water}}^{\mathrm{G,if}}\right) - C_{\mathrm{tot}}^{\mathrm{G}}\left(D_{11}\frac{dy_{\mathrm{methanol}}}{dz} + D_{12}\frac{dy_{\mathrm{water}}}{dz}\right) \tag{22}$$

$$N_{\mathrm{water}}^{\mathrm{G,if}} = y_{\mathrm{water}}\left(N_{\mathrm{methanol}}^{\mathrm{G,if}} + N_{\mathrm{water}}^{\mathrm{G,if}}\right) - C_{\mathrm{tot}}^{\mathrm{G}}\left(D_{21}\frac{dy_{\mathrm{methanol}}}{dz} + D_{22}\frac{dy_{\mathrm{water}}}{dz}\right) \tag{23}$$

where the first term of the right-hand side of this equation represents the convective flux and the second term stands for the molecular diffusion, and D_{ij} are calculated from $[\mathrm{D}] = [\mathrm{B}]^{-1}$ (cf. Ref. 19).

The following assumptions are made to transform and integrate Eqs. 22 and 23 (see Appendix):

1. Due to the fact, that the nitrogen concentration in the membrane pore is much higher than that of methanol and water, the concentration change of nitrogen along the pore length is neglected.

2. Diffusion coefficients D_{ij} in Eqs. 22 and 23 are assumed constant in line with the linearized theory (cf. Refs. 19,20).

Furthermore, assuming a uniform pore distribution across the membrane, the methanol and water mass flux description in a single pore is extended to govern the whole membrane domain. This is done by multiplying the integrated mass flux equations (Eqs. A14 and A15) from Appendix) by the membrane porosity ε.

At the inlet boundaries of the channels (B in Figure 3b), molar concentrations were defined as follows

$$x_{i,\mathrm{inlet}} = x_{i,0} \tag{24}$$

The diffusion flux at the outlet boundaries of the channels (C in Figure 3b) was neglected as it is small compared to the respective convective flux

$$N_{\mathrm{out}} = \vec{\mathrm{n}} \cdot \left(-C_{\mathrm{tot}}^{L} D^{L} \nabla x_i\right) = 0 \quad \text{(binary system)} \tag{25}$$

$$N_{\mathrm{out}} = \vec{\mathrm{n}} \cdot \left(-C_{\mathrm{tot}}^{\mathrm{G}} [\mathbf{B}]^{-1} \nabla \mathbf{y}\right) = 0 \quad \text{(ternary system)} \tag{26}$$

Finally, all walls (A in Figure 3b) were considered to be impermeable

$$N_{\mathrm{wall}} = \vec{\mathrm{n}} \cdot \left(-C_{\mathrm{tot}}^{L} D^{L} \nabla x_i + C_{\mathrm{tot}}^{L} \vec{\mathrm{u}} x_i\right) = 0 \quad \text{(binary system)} \tag{27}$$

$$N_{\mathrm{wall}} = \vec{\mathrm{n}} \cdot \left(-C_{\mathrm{tot}}^{\mathrm{G}} [\mathbf{B}]^{-1} \nabla \mathbf{y} + C_{\mathrm{tot}}^{\mathrm{G}} \vec{\mathrm{u}} \mathbf{y}\right) = 0 \quad \text{(ternary system)} \tag{28}$$

Implementation

The system of model equations described above was solved with the commercial CFD tool COMSOL Multiphysics by COMSOL AB,[21] which is based on the finite element method. To obtain the numerical approximation of the integral resulting from Eqs. 22 and 23, the Simpson rule was used. The diffusion coefficients for binary feed mixtures were first determined at infinite dilution using the Wilke–Chang method and afterward adjusted for concentrated solutions with the Hsu–Chen method.[22] For the ternary gas-phase system, the binary Stefan–Maxwell diffusion coefficients were calculated using the Wilke–Lee method.[22] The saturation pressure of the pure components was determined using the Antoine's equation, and the activity coefficients were calculated using Wilson's model.[23]

After implementation of the equations and boundary conditions, a grid independence study was performed. To achieve grid-independent results, altogether 1,200,000 hexagonal elements were found to be necessary for the entire computational domain.

Results and Discussion

Model validation

The simulations were performed for the operating conditions of the experimental study presented in Ref. 16 to validate the model and solution method. The comparison between the simulations and measurements were made for the resulting overall mass flux of evaporated methanol and water through the membrane and the separation factor with respect to methanol. The effect of the following parameters was investigated:

1. Variation of the feed composition and temperature.
2. Variation of the inert gas volumetric flow rate.
3. Three different membrane types presented in Table 1.

In all cases, the inlet temperature of the inert gas nitrogen was about 22°C and the inlet concentrations of methanol and water in the inert gas were equal to zero.

A comparison between the simulation results and the experimental data was done for the following different cases: for the membrane of type PES40, the total mass fluxes were compared at a feed temperature of 51°C (Figure 4a) and for the membranes of type PES40 and type PVDF22 at a feed temperature of 60°C (Figure 4b) while feed compositions were varied. In Figures 5a, b, a comparison of the separation factors is shown for the same process conditions and membrane types. In Figure 6, the total mass fluxes are compared for different inert gas volumetric flow and the membrane of type ePTFE45, and for the same conditions, the separation factors are compared in Figure 7. As can be seen from these comparisons, the numerical and experimental results are in a good agreement. The developed model is able to capture the effects of different process conditions as well as the impact of different membrane types. In particular, the following tendencies found experimentally[16] could be confirmed. Increasing methanol concentrations in the feed lead to growing total mass fluxes through the membrane due to a higher amount of evaporating methanol. At a higher feed temperature, both methanol and water evaporate with higher rates because of increased partial vapor pressures. Growing inert gas volumetric flow rates cause first a rise of the total mass flux which, however, slightly decreases at very high-flow rates. On the one hand, at increased gas velocity, the evaporated methanol and water are swept away out of the gas channel with a higher rate. As a result, a higher concentration difference between the gas channel and the membrane pores arises. This means an enhanced mass-transfer driving force and, consequently, rising mass flux of evaporating methanol and water. On the other hand, pressure in the gas channel rises with the gas velocity, as a higher inlet pressure is required to overcome the pressure drop in the channel. Thus, the evaporation rate of methanol and water reduces. This effect dominates at the highest inert gas velocities, and the mass flux drops. It can also be seen that the membrane PES40 with lowest porosity of 0.55 yields the lowest total mass fluxes. A detailed discussion on these effects is given in Ref. 16. The average deviation for all data is about 11%. Higher deviations mostly appear at feed temperatures exceeding 60°C and can be attributed to heat losses in the microseparator which can hardly be taken into account by the modeling.

Determination of Mass-Transfer Resistance. To examine the mass-transfer characteristics of the membrane distillation process described above, mass-transfer resistances in the gas and feed channels and in the membrane were determined for methanol. The overall gas-side mass-transfer resistance was defined as

$$\frac{1}{k^{\mathrm{G}}_{\mathrm{methanol}}} = \frac{1}{\beta^{\mathrm{G}}_{\mathrm{methanol}}} + \frac{1}{\beta^{\mathrm{M}}_{\mathrm{methanol}} \cdot \varepsilon} + \frac{b}{\beta^{L}_{\mathrm{methanol}}} \tag{29}$$

where b is distribution coefficient. The first term in the right-hand-side represents the resistance of the gas phase in the gas channel, the second the resistance of the gas phase in the membrane pores, and the third term represents the resistance of the liquid phase in the feed channel. Due to the relatively low fluxes of evaporating methanol and water, the feed composition changes only slightly along the channel length. Consequently, parameter b is nearly constant and can be determined as an average value for the channel length. The mass-transfer coefficients in Eq. 29 were calculated according to

$$\beta_{\mathrm{methanol}} = \frac{N^{\mathrm{if}}_{\mathrm{methanol}}}{\Delta C_{\mathrm{methanol}}} \tag{30}$$

The concentration limits in Eq. 30 are defined for both sides of the membrane, between the respective membrane surface and the channel wall. In the vapor phase, there are two resistances, and hence, there exist two mass-transfer coefficients, one in the membrane and one in the gas channel.

In Figure 8, the individual mass-transfer resistances are shown for the three membrane types under study for a liquid volumetric flow rate of 8 mL min^{-1} and a gas volumetric flow rate of 49 mL min^{-1}.

As can be seen, the resistance distribution differs for different membrane types. The main mass-transfer resistance for the PES40 membrane is located in the membrane pores. In contrast, for the membrane types PVDF22 and ePTFE45, higher resistances in the gas and feed channels are found. These membranes have a high porosity of 0.75 and 0.91, whereas the PES40 membrane porosity is only about 0.55. On the other hand, the thickness of this membrane is 166 μm, which is lower than the thicknesses of ePTFE45 (250 μm). Thus, we may conclude that the mass transfer in the membrane is rather determined by its porosity than by its thickness. This agrees with the experimental results presented in Ref. 16 where considerably higher mass fluxes of the methanol/water mixture could be observed for the membrane ePTFE45. Membrane PVDF22 has a relative high porosity and low thickness (116 μm), and this results in mass fluxes comparable to those of membrane ePTFE45.

Mass-transfer intensification by miniaturization

A further aim of our numerical analysis was to develop geometric improvements of the apparatus to intensify the process. The latter is only efficient for membrane types with lower mass-transfer resistance. The membranes ePTFE45 and PVDF22 fulfill this condition. They show a similar performance. However, the membrane PVDF22 demonstrates a higher process stability concerning the liquid entry pressure (Table 1). Therefore, it was selected for the intensification study. In our first investigations, the effect of a further miniaturization of the separation unit was studied numerically. As can be seen in Figure 8, the highest mass-transfer resistance of the process with the membrane PVDF22 is located in the liquid channel. Therefore, the effect of the liquid channel height reduction on the mass transfer was investigated. The height was reduced stepwise from 1 to 0.1 mm.

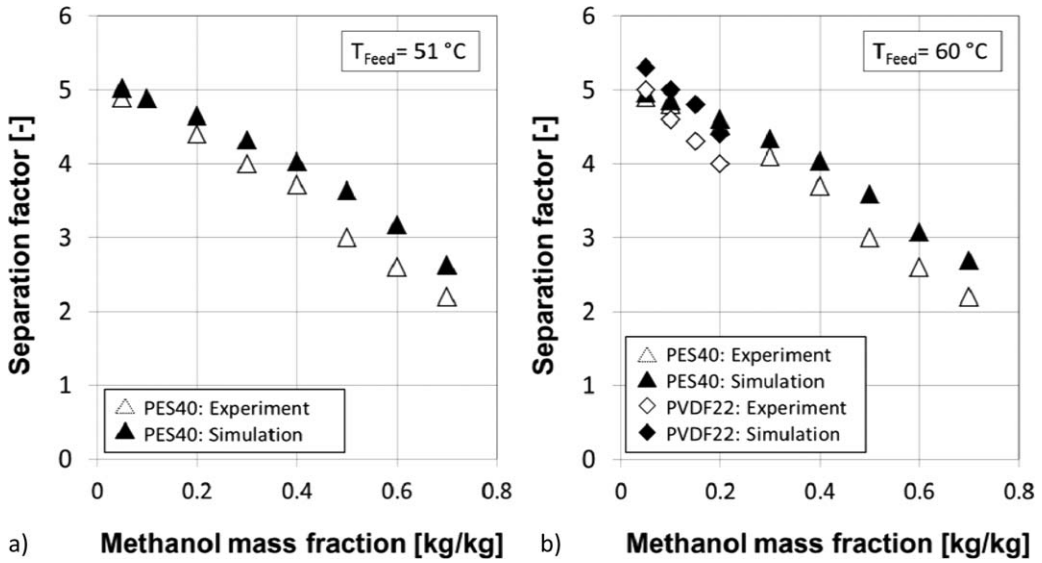

Figure 5. Comparison of the simulated and measured separation factor with respect to methanol for different feed compositions and the inlet temperatures of 51°C (a) and 60°C (b) for the membrane of type PES40 and PVDF22.

For all simulations, the inlet feed velocity was kept constant at 0.27 m s^{-1}. The simulation results illustrated in Figure 9a show that the mass-transfer resistance in the feed channel reduces due to shorter diffusion path. For a half-height channel, it is already below the resistance of the gas channel and the membrane. However, the reduced channel heights result in increased pressure drop (Figure 9b). Especially at channel heights below 0.2 mm, the pressure drop is about one order of magnitude higher compared to that of the original height (1 mm). In this case, the pressure in the feed channel exceeds the liquid entry pressure of the membrane and leads to a breakthrough of the liquid. Consequently, at channel dimensions below 0.2 mm, the microseparator can no longer be operated.

Mass-transfer intensification by baffles

Another way toward process intensification is the use of baffles in the microchannel. Their effect on the enhancement of the heat and mass transfer at mesoscale was already investigated in several works.[24–30] Moreover, investigations on baffles inside microchannels were carried out in Refs. 31-34. In these works, rigid elements of different shape were used to induce flow separation and recirculation in the apparatus. Thereby, the convective transport was facilitated. Often, the induced flow is clearly 3-D. However, for several fluid separation processes, in which the concentration gradient is directed mainly in one direction, namely perpendicular to the phase interface, purely 2-D flow deflection can be efficient. In this case, a baffles profile is required by which the flow is redirected toward the phase interface. In contrast, 3-D flow deflection and recirculation would lead to useless energy dissipation.

Along these lines, we developed a new baffle geometry ensuring an efficient mass-transfer performance. The baffle design largely depends on the manufacturing. The baffle geometry suggested in this work was intended to be manufactured by 3-D printing. To ensure a high accuracy of the geometry, the thickness of the baffle profile was limited to a minimal size of 0.6 mm. The cross-section of the

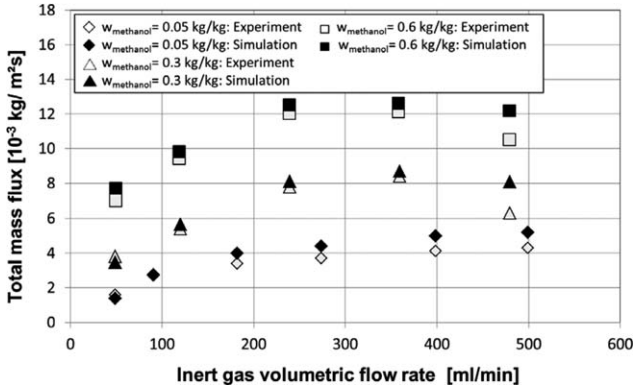

Figure 6. Comparison of the simulated and measured mass fluxes of the methanol/water mixture through the membrane for different inert gas volumetric flow rates at a feed temperature of 60°C for the membrane of type ePTFE45.

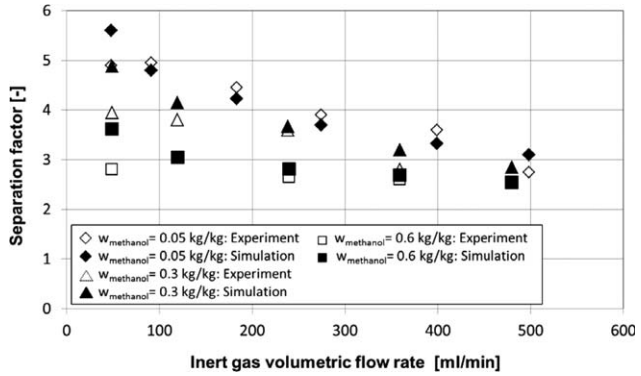

Figure 7. Comparison of the simulated and measured separation factors for different inert gas volumetric flow rates at a feed temperature of 60°C for the membrane of type ePTFE45.

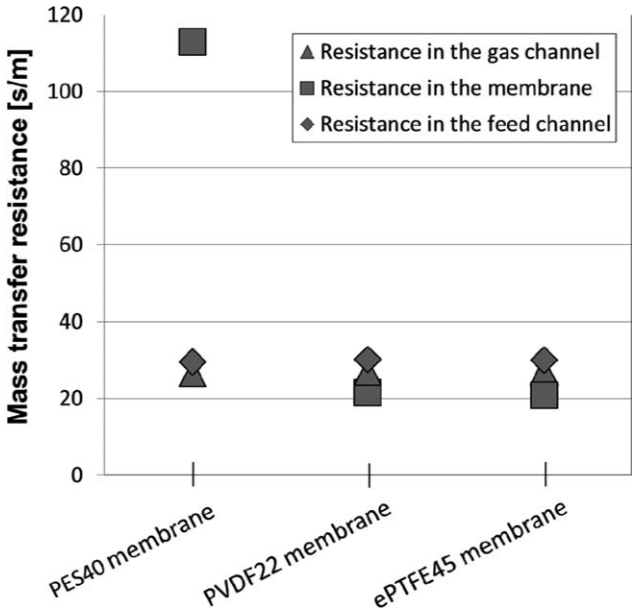

Figure 8. Distribution of the mass-transfer resistance for the three membrane types under study.

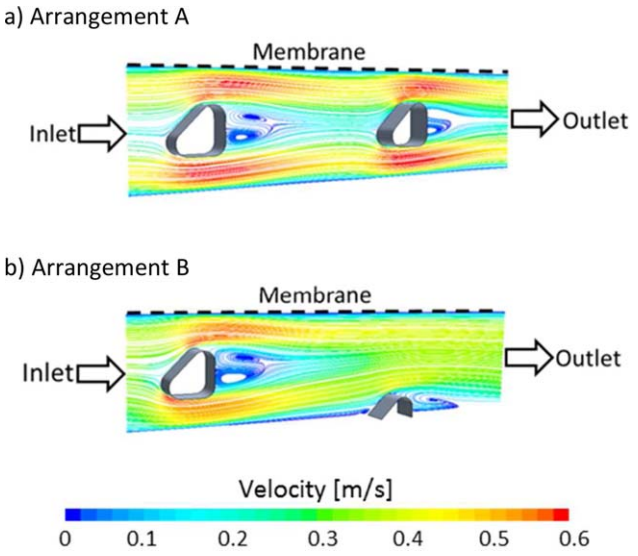

Figure 10. Representative section of the feed channel with two different baffle arrangements: arrangement A: both baffles in the middle of the channel height (a); arrangement B: second baffle at the bottom of the channel (b).

[Color figure can be viewed in the online issue, which is available at wileyonlinelibrary.com.]

microchannel under study is too small to fulfill this condition. Therefore, the channel cross-section was enlarged from 1×0.5 to 3×1.5 mm^2. The first baffle design for the feed channel is shown in Figure 10a. The height of the baffle profile is equal to one third of the channel height. The front is tilted 45° to the phase interface. The distance between two baffles is equal to 6 mm. This is sufficiently long to ensure that the second baffle does not border directly the wake region arising due to the first baffle. Too short distances would prevent any acceleration of the flow behind the wake region and lead to the second baffle being enveloped by wakes. Although the wake flow pattern reveals a recirculation, the velocity in this region is nearly equal to zero, and hence, there is practically no mass and heat transfer by convection.

Two different baffle arrangements (Figures 10a, b) were investigated with respect to the fluid dynamics and mass transfer. In the first arrangement (arrangement A; Figure 10a), both baffles are on the same level in the middle of the channel height. In the second arrangement (arrangement B; Figure 10b), the second baffle is placed at the bottom of the channel. Both arrangements possess a certain periodicity. The stream lines shown in Figure 10 are obtained in the simulations of the liquid-phase flow for the inlet velocity of 0.27 m s^{-1}.

For both baffle arrangements, flow redirections with separation and wake formation behind the baffle profile are visible. The effect of these flow deflections on the mass transfer was evaluated by comparing the mass-transfer coefficients with those of the microchannels without baffles. The latter include the miniaturized channels investigated in the

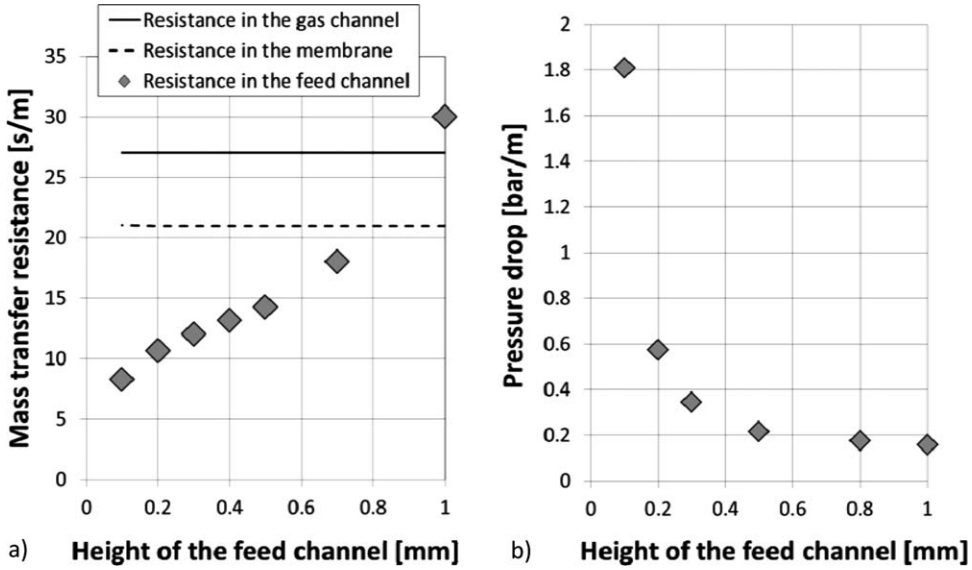

Figure 9. Impact of the feed channel height on the mass-transfer resistance (a) and the pressure drop (b).

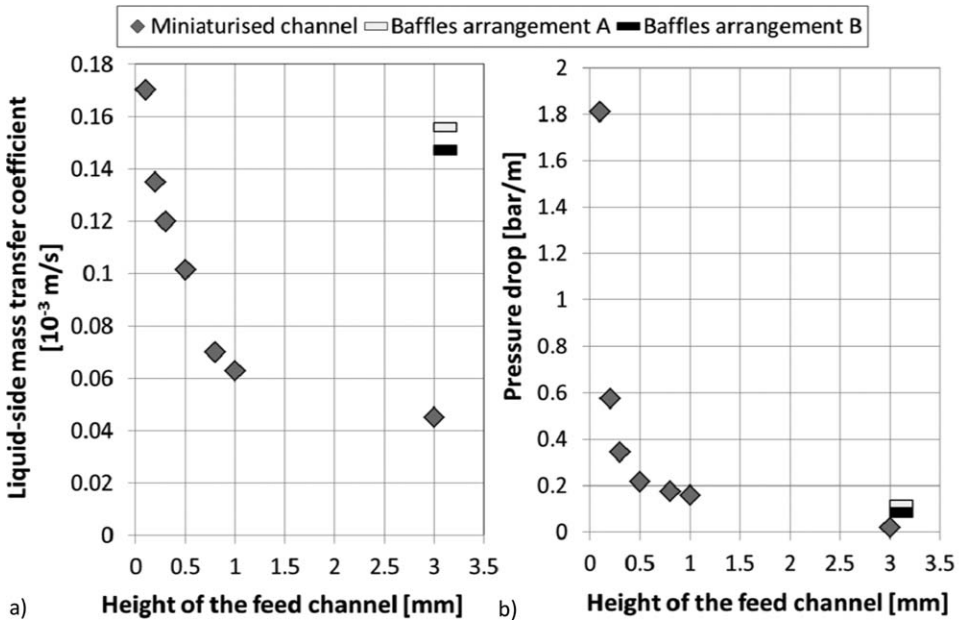

Figure 11. Mass-transfer coefficient (a) and pressure drop (b) of the feed channel determined for miniaturized channels as well as for the baffle arrangements A and B.

previous section. The comparison is shown in Figure 11a. The highest values of the mass-transfer coefficients can be obtained in the channel with baffles and in the miniaturized channel of 0.1 and 0.2-mm height. Clearly, the flow deflection caused by the baffles leads to an intense mixing by which the mass transfer is intensified in a similar way as by reducing the diffusion paths. The mass-transfer coefficient of the arrangement A is about 5% higher than that of the arrangement B. This can be attributed to the second baffle in the arrangement A which is placed in the middle of the channel and causes an upward and downward flow redirection. In contrast, in the arrangement B, the second baffle placed on the channel bottom redirects the flow only upward. However, the downward flow redirection is relatively low and the mixing effect is insignificant.

Along with the mass-transfer coefficient, pressure drop represents an important characteristics of the microapparatus. Consequently, the simulated pressure drop values for the different channel geometries are compared in Figure 11b. By far the highest pressure drop is caused by the miniaturized channels. Their small cross-section leads to a high-wall friction. In contrast, the channels with baffles show low-pressure drop values, although a considerable flow resistance is induced by the baffles. These values are even lower than those of the original channel geometry with 1-mm height. Furthermore, the baffle arrangement B has an about 30% lower flow resistance than the arrangement A, despite comparable mass-transfer coefficients. Consequently, the channel geometry with the baffle arrangement B demonstrates the best performance regarding the mass-transfer intensification and pressure drop.

With the baffles arrangement B taken as a basis, further investigations were performed. As can be seen in Figure 10, the baffle results in a relatively large wake region which causes useless energy dissipation. This region can be reduced by appropriate geometrical improvements. Therefore, the point at which the flow separates from the baffle was identified and, beginning from this point, the baffle shape was elongated backward. The modified baffle geometry with the corresponding stream lines is shown in Figure 12. As can be seen, the resulting wake region is considerably smaller than in Figure 10. The effect of this modification on the pressure drop and the mass-transfer coefficient is shown in Table 2 in which both characteristics are listed for the modified baffle geometry and the initial one. The reduction of the wake region leads to an about 20% lower pressure drop. In contrast, the mass-transfer coefficient is barely affected by the geometrical modification. It is only about 5% lower than that of the initial geometry.

Investigation of the Modified Microseparator

The analysis presented above shows that mass transfer in the microseparator under study can be intensified both by miniaturization and the use of baffles. Further, the baffles provide significantly lower pressure drop compared to both the original and miniaturized channel geometry. If an appropriate geometry of the baffle is found, flow separation and wake formation in the back of the baffle profile can be kept on a low level. This perspective motivated us to extend the

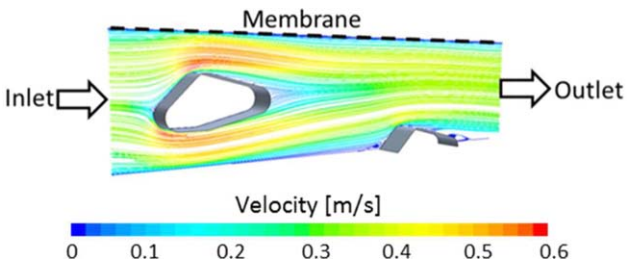

Figure 12. Representative section of the feed channel with baffle arrangement B and improved baffle geometry.

[Color figure can be viewed in the online issue, which is available at wileyonlinelibrary.com.]

Table 2. Mass-Transfer Coefficient and Pressure Drop of the Original Feed Channel, the Initial Baffle Arrangement B, and the Modified Baffle Arrangement

Geometry	Liquid-Side Mass-Transfer Coefficient (m/s)	Pressure Drop (bar/m)
Original channel with 1-mm height	7×10^{-5}	0.16
Channel with initial baffle geometry of arrangement B and 3-mm height (Figure 10b)	1.47×10^{-4}	0.08
Channel with modified baffle geometry of arrangement B and 3-mm height (Figure 12)	1.4×10^{-4}	0.065

analysis of the mass-transfer intensification by baffles. In a subsequent study, the impact of baffles was investigated not only with respect the mass transfer in the feed channel but also regarding the gas channel, for different feed and gas inlet velocities.

The final baffle geometry presented in Figure 12 was used for the design of a new microseparator. This new device consists of two plates made of a photopolymer resin (Figures 13a, b). The plates were manufactured by 3-D printing at Object GmbH. On one plate, a microchannel incorporating the modified baffle profiles is placed. The microchannel placed on the second plate has no baffles. The two plates are screwed together, with the membrane PVDF22 between them.

With the new apparatus geometry, experiments and simulations were carried out to validate the developed model for this complex channel geometry. For the experiments, the setup presented in Ref. 16 and shown in Figure 2 was used. With the exception of the new microseparator, all other components of the setup remained unchanged. The experimental procedure corresponded to that described in Process Description section.

Two experimental studies were carried out with the new apparatus. In the first study, the feed was led in the channel with baffles while the feed volumetric flow rate varied between 20 and 70 mL min^{-1}. The inert gas flowed countercurrently through the channel without baffles. Its volumetric flow rate was kept at 1000 mL min^{-1}. In the second study, the inert gas was led in the channel with baffles at different volumetric flow rates (200–800 mL min^{-1}) while the feed flowing through the other channel had a flow rate of 50 mL min^{-1}. To reduce possible deviations between the experiments and simulations resulting from heat losses, the inlet temperature of the feed was kept at a relatively low level, namely, 45°C. In all studies, the methanol mass fraction in the feed was equal to 0.18 kg/kg. Similarly to Ref. 16, total mass flux of the methanol/water mixture through the membrane was determined by collecting and weighing the permeate in the ice bath cooler after a certain time interval in the experiment. Furthermore, the separation factor was calculated based on the methanol concentration in the permeate, which was determined by gas chromatography.

The simulations were carried out for the same operating conditions as in the experiments. The resulting total mass fluxes and separation factors of the experimental and numerical studies were compared. This comparison is illustrated by a parity plot in Figure 14. As can be seen, a good agreement, with the average deviation of 7%, was achieved.

With the validated model, further simulation studies were carried out to evaluate the performance of the new apparatus geometry. Due the limitation on the minimal baffle size by the manufacturing process, the channel height of the new geometry (3 mm) is larger than that of the original geometry (1 mm). Therefore, it was interesting to evaluate the baffles influence based on the same channel height of 3 mm. Consequently, we preformed additional simulations without baffles. Furthermore, the performance of the miniaturized channel geometry with 0.2-mm height was included in the comparison.

For the four geometries listed in Table 3, two simulation studies were performed. In the first study, the effect of the feed inlet velocity on the liquid-side mass-transfer coefficient and pressure drop was investigated. The feed inlet velocity was varied between 0.04 and 2.6 m s^{-1} while the inert gas inlet velocity was kept at 3.7 m s^{-1}. The baffles were placed only in the feed channel for this investigation. In the second study, the effect of the gas inlet velocity on the gas-side mass transfer and pressure drop was determined. In this case, the feed inlet velocity was kept at 0.18 m s^{-1} while the inert gas inlet velocity was varied between 0.74 and 3.7 m s^{-1}. Furthermore, the baffles were placed in the gas

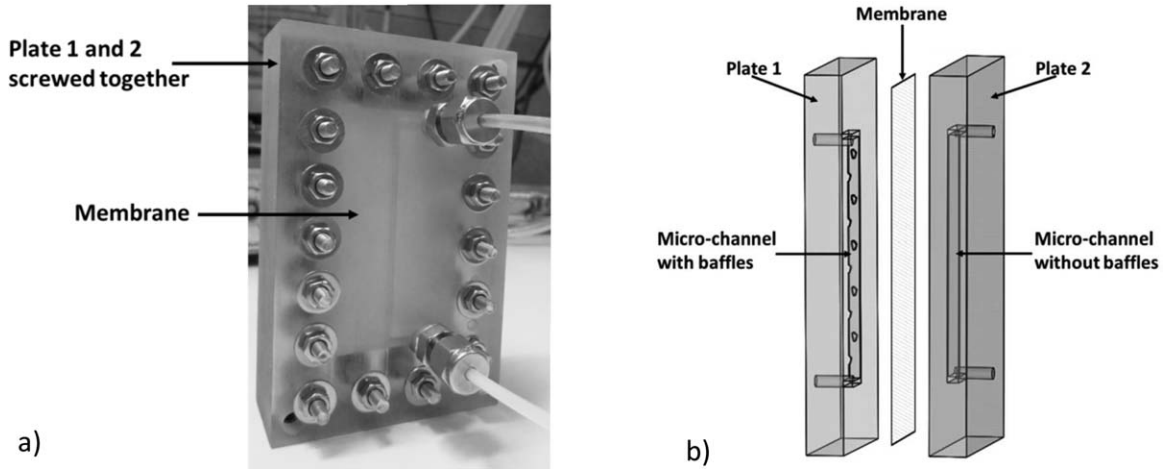

Figure 13. Photography of the microseparator consisting of two plates with microchannels and a membrane (a); CAD-drawing of the two plates with microchannels (b).

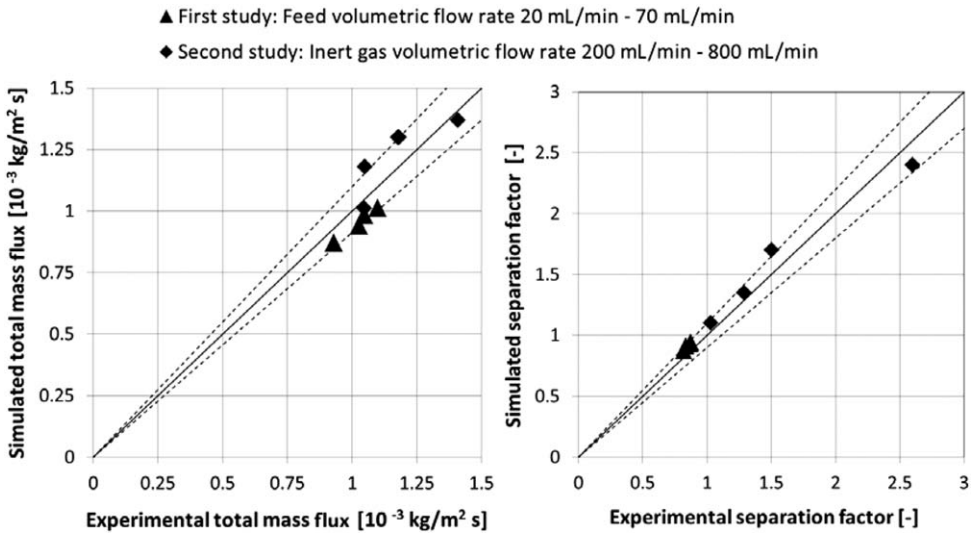

Figure 14. Model validation with experimental results for different feed and gas inlet velocities.

channel. For all simulations, the feed inlet temperature was kept at 45°C and the feed methanol concentration at 0.18 kg/kg.

Impact of the feed inlet velocity on the liquid-side mass-transfer coefficient

In Figure 15, the values of the liquid-side mass-transfer coefficient for different feed inlet velocities are shown. For all channel geometries, they increase with the feed velocity. For the three channels without baffles, this behavior can be compared to the mass-transfer coefficient resulting from a fully developed laminar flow with not fully developed concentration profile in a relatively short pipe. This coefficient can be described by the following Sherwood correlation[35]

$$Sh = \frac{\beta\delta}{D_i} = 1.61\left(Re\,Sc\,\frac{d}{L}\right)^{1/3} \tag{31}$$

where δ is characteristic length for the mass transfer, d is pipe diameter, and L is pipe length. In relative short pipes, the concentration profile is not yet fully developed. In this case, the Sherwood number or mass-transfer coefficient increases with rising Reynolds number according to Eq. 31. Despite the considerable length of the microchannels under study (70 mm), no fully developed concentration profiles could be obtained in the simulations. This can be attributed to the changing equilibrium concentration at the interface related to the countercurrent flow of the feed and gas. The effect of the channel height on the mass-transfer coefficient is also comparable with that given by the Sherwood correlation, Eq. 31.

Table 3. Channel Geometries Used for the Simulation Studies; All Channels have a Length of 70 mm

Channel Height	Remark
0.2 mm	Miniaturized channel
1 mm	Original channel
3 mm with baffles	Enlarged channel according to the conditions of the manufacturing process; baffle arrangement B with optimized baffle profile
3 mm	Enlarged channel without baffles used for comparison with the above channel

The mass-transfer coefficient in the channel with baffles is nearly twice as high as those in the channels of 1 and 3-mm height without baffles (Figure 15). This can be explained by the reduced concentration gradients caused by the flow deflection. However, the mass-transfer coefficient values for the miniaturized channel (0.2 mm) are somewhat higher at lower feed velocities. In this case, the shorter diffusion path of 0.2 mm leads to a slightly better mass-transfer performance than the effect of the flow deflection. At higher feed velocities, the flow deflection in the channel with baffles becomes significant and its performance is superior to the performance of the miniaturized channel.

Impact of the gas inlet velocity on the gas-side mass-transfer coefficient

The impact of the gas inlet velocity on the gas-side mass-transfer coefficient (determined according to Eq. 30 for the gas channel) is shown in Figure 16. For the channel of 3-mm height, this coefficient increases with increasing Reynolds number. In contrast, the channels of 1 and 0.2-mm height show almost constant coefficients. In these channels, the residence time of the gas is longer than the time required for the species to diffuse from the interface to the wall. This concerns even the high gas inlet velocities. The characteristic

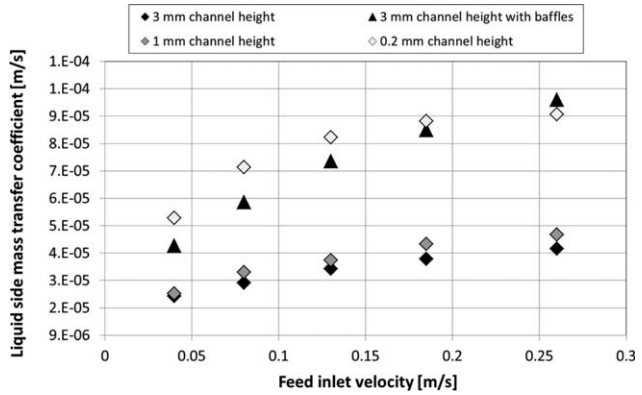

Figure 15. Effect of the feed inlet velocity on the liquid-side mass-transfer coefficient.

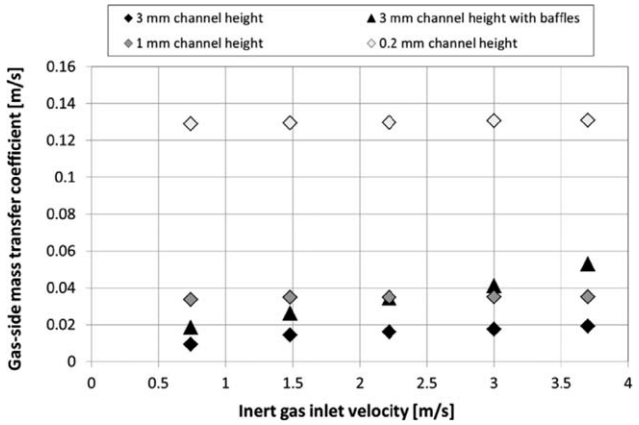

Figure 16. Impact of the inert gas inlet velocity on the gas-side mass-transfer coefficient.

diffusion time can be estimated from the Einstein–Smoluchowski equation[36]

$$t = \frac{\bar{x}^2}{2D_i} \tag{32}$$

where t is time taken for the square displacement, $\bar{x}^2$, of a molecule by diffusion. For the channel of 1-mm height, the time t equals 0.03 s for the diffusion of methanol from the interface to the wall. The residence time of the gas phase in this channel is equal to 0.09 s for the highest inlet velocity of 3.7 m s^{-1}.

The resulting concentration profile of methanol in the gas channel is illustrated in Figure 17a. Near the gas channel inlet, a concentration change from the interface to the wall is visible; it disappears near the outlet due to the uniform distribution of methanol by diffusion. In Figure 17b, the corresponding concentration profile in the feed channel is shown. In contrast, a steep concentration decrease is still visible at the outlet of the feed channel.

Increasing the gas channel height from 1 to 3 mm leads to an about one order of magnitude longer diffusion time which now exceeds the residence time. The resulting concentration profile is shown in Figure 18a. Near the gas channel inlet and the channel outlet, a strong concentration decrease from the phase interface toward the wall is visible.

The channel of 3-mm height with baffles shows a better mass-transfer performance than the identical channel without baffles (cf. Figure 16). The reduction of the concentration gradient due to the flow deflection is more significant than due to diffusion. At lower channel heights, however, diffusion paths become shorter and the role of diffusion grows. Therefore, at low-gas velocities, the channel of 1-mm height leads to higher mass-transfer coefficients than the channel with baffles. However, with rising gas velocity, mass-transfer coefficients in the channel of 1-mm height remain almost constant, whereas those in the channel with baffles increase due to stronger flow deflection.

The mass-transfer coefficients of the narrowest channel (0.2-mm height) are almost one order of magnitude higher than those of all other channel geometries (Figure 16). The combination of a relatively high diffusion coefficient in the gas phase and a very short diffusion path leads to a significantly better mass-transfer performance than in the wider channel with baffles. This effect could not be evidenced for the feed channel due to the considerably lower diffusion coefficients.

Impact of the feed and gas inlet velocity on the overall gas-side mass-transfer coefficient

After evaluating the individual mass-transfer coefficients in the gas and liquid phase, we came back to the overall mass-transfer coefficient defined by Eq. 29. As already mentioned, mass transfer is determined not only by the feed channel and gas channel but also by the membrane. Thus, the mass-transfer intensification studied here is reasonable only for membranes with relatively low resistance. To evaluate the mass-transfer enhancement in the microseparator under study, the overall gas-side mass-transfer coefficient was determined. In Figure 19, this coefficient is shown for the channels of 0.2, 1, and 3-mm height as well for the channel of 3-mm height with baffles, for different feed and inert gas inlet velocities. As can be seen in Figure 19a, the overall

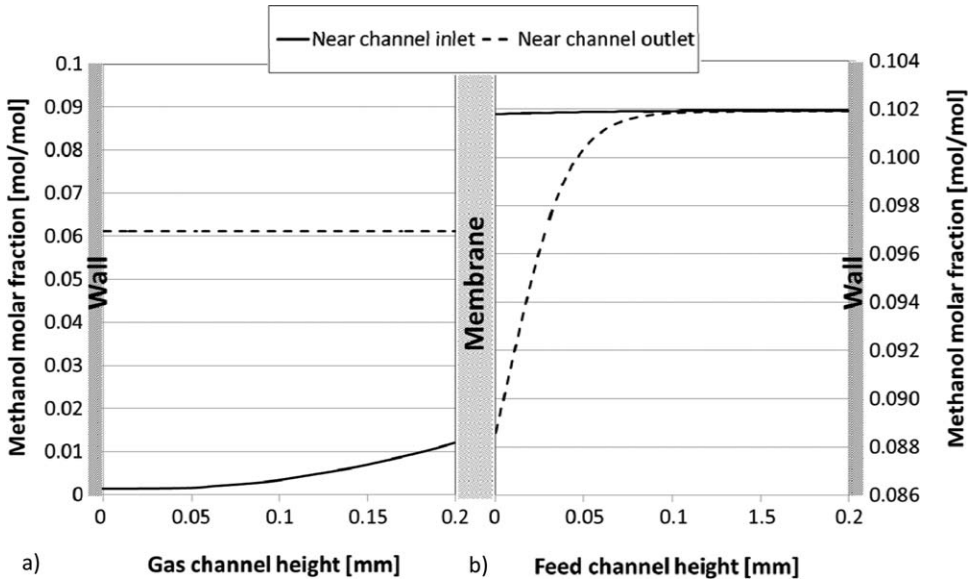

Figure 17. Methanol molar fraction profile normal to the phase interface in the gas channel (a) and in the feed channel (b) for channel height of 0.2 mm.

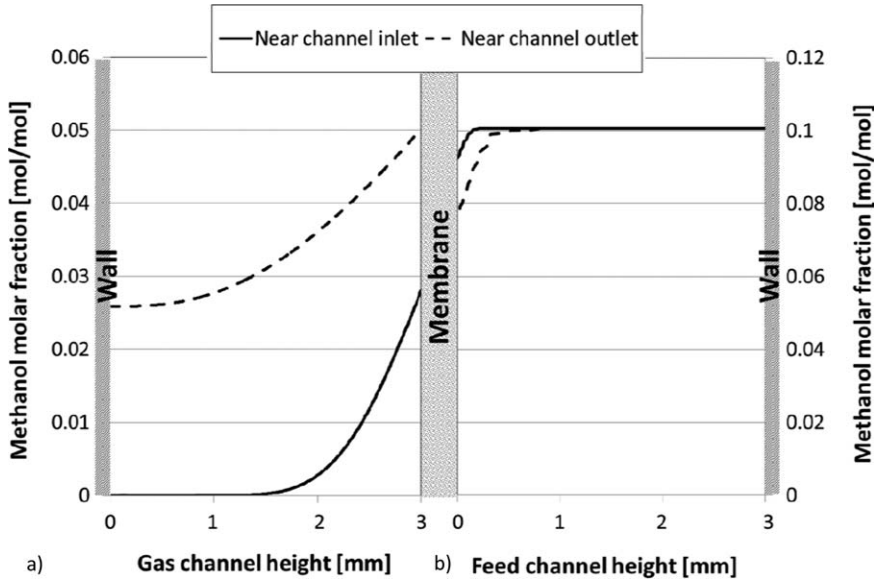

Figure 18. Methanol molar fraction profile normal to the phase interface in the gas channel (a) and in the feed channel (b) for a channel height of 3 mm without baffles.

coefficient increases with the feed velocity for all four geometries, due to the increase of the liquid-side mass-transfer coefficient. Both the miniaturization of the channels and the use of baffles lead to a higher performance of the microseparator. A similar tendency can be seen in Figure 19b. In this case, however, the overall coefficients for the channels of 1 and 0.2-mm height are not affected by the increase of the gas velocity due to the constant gas-side mass-transfer coefficients.

Impact of the feed and gas inlet velocity on the pressure drop

The performance of the four channel geometries under study was also evaluated with respect to the corresponding pressure drop. In Figure 20, the pressure drop in the feed and in the gas channel is shown as a function of the feed and gas inlet velocity. As expected, the widest channel of 3-mm height without baffles has the lowest pressure drop. The same channel with baffles leads to higher pressure drop due to higher flow resistance yet showing lower pressure drop than the channel of 1-mm height (original channel). The pressure drop in the narrowest channel of 0.2 mm is by far the highest.

In summary, feed channels which were modified by miniaturization or by the use of baffles provide mass-transfer intensification with comparable overall gas-side mass-transfer coefficients for both modifications. Similar modification of the gas channel rather enhances mass transfer in miniaturized channel. However, the channel with baffles shows a steep rise of the mass-transfer coefficient with increased gas

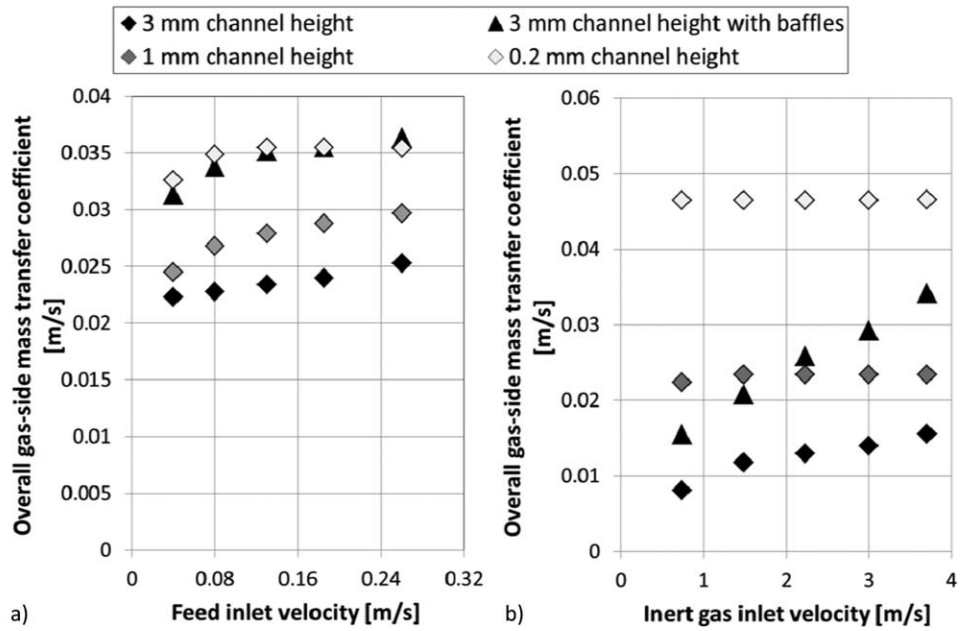

Figure 19. Impact of the feed inlet velocity (a) and inert gas inlet velocity (b) on the overall gas-side mass-transfer coefficient.

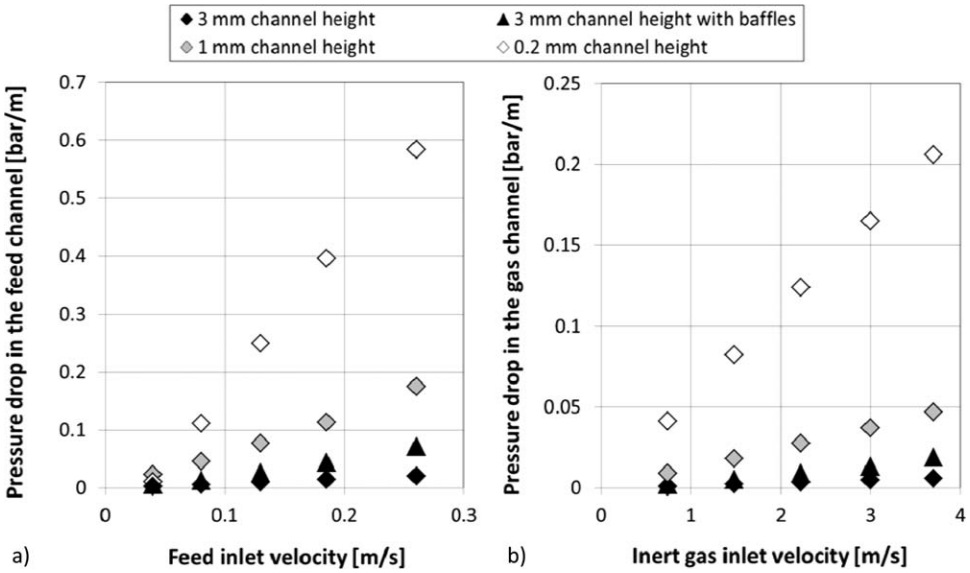

Figure 20. Impact of the feed inlet velocity on the pressure drop in the feed channel (a) and impact of the inert gas velocity on the pressure drop in the gas channel (b).

velocity, and at high velocities, it comes closer to that of the miniaturized channel. Furthermore, a channel with baffles causes about one order of magnitude lower pressure drop and permits significantly higher throughputs than the miniaturized channel. Consequently, the following different designs of a separation unit can be suggested depending on the process conditions:

1. For a separation process largely limited by the liquid-side mass transfer, the use of baffles in the liquid channel is recommended, as this results in a considerable enhancement of the liquid-side mass transfer at relatively low pressure drop.

2. For a process largely limited by the gas-side mass transfer, the use of a miniaturized gas channel will lead to strong mass-transfer enhancement yet at relatively high pressure drop.

3. For processes in which pressure drop represents a strong limiting factor, whether in the liquid channel or in the gas channel, the channel geometry with baffles represents a more reasonable option.

Concerning the membrane distillation process investigated in this work, we have to do just with the latter case, with respect to both the feed and the gas channel. On the one hand, the liquid entrance pressure of the membrane limits the allowed pressure drop in the feed channel. On the other hand, the methanol and water evaporation rates may be significantly reduced due to a high inlet pressure in the gas channel, this high pressure is nevertheless required to overcome significant pressure drop in a miniaturized channel.

Conclusions

In this work, the membrane distillation of methanol and water in a microseparator designed by Adiche and Sundmacher [16] was investigated experimentally and numerically. This unit consists of gas feed and liquid feed microchannels separated by a hydrophobic membrane. A rigorous 3-D model was developed including the liquid-phase and gas-phase fluid dynamics and a coupled heat and mass transfer description. This detailed description takes into account the transport phenomena in both channels as well as inside the membrane and represents a novel and universal modeling approach for arbitrary micromembrane distillation units.

With the developed model, simulation studies for different operating conditions and three membrane types were carried out and the resulting total mass flux of evaporated methanol and water as well as the separation factor were compared with the experimental data from Ref. 16. Good agreement between the simulation results and experimental data was found. The results obtained from the simulation studies were used to determine the mass-transfer resistance in the gas and feed channel and in the membrane. For the membrane type with lowest porosity of about 0.55, the main mass-transfer resistance was located in the membrane. In contrast, for membranes with porosities of 0.75 and 0.91, higher resistances were found in the feed and the gas channel. On the other hand, the membrane with porosity of 0.91 has the highest thickness of the three membrane types. This indicates that the mass transfer in the membrane is rather dominated by its porosity than by its thickness under the investigated process conditions.

Two different ways for mass transfer intensification in the gas and in the liquid channels were investigated numerically. First, the channel height was reduced from 1 up to 0.2 mm. This significantly reduced the diffusion path toward the phase interface. For the second way, baffles were placed in the channel to induce flow deflection. Particular attention was given to the design of the baffle profile. The front of the profile was tilted 45° to the phase interface to redirect the flow normally to the interface. Its back was elongated to reduce the wake formation. The baffle minimal size of 0.6 mm was limited by the manufacturing process. As the original channel cross-section is too small for the minimal baffle size, it was enlarged from 1×0.5 to 3×1.5 mm^2. This new channel geometry was used for the design of a new microseparator with which experiments were carried out to validate the developed model with the new geometry. For different inert gas and feed volumetric flow rates, good agreement between the simulated and measured total mass fluxes and separation factors was obtained.

With the original channel geometry, the miniaturized channel and the enlarged channel with baffles, simulation studies were carried out to investigate the effect of the gas and feed inlet velocity on the gas-side and liquid-side mass-transfer coefficient and on the pressure drop. For both the liquid-side and gas-side

mass transfer, the miniaturized channel and the channel with baffles led to mass-transfer enhancement. While for both geometries, similar liquid-side mass-transfer coefficients could be obtained, significantly higher gas-side mass-transfer coefficients were found for the miniaturized channel. As the effective diffusion coefficients of methanol and water in the gas phase are about 10^4 higher than in the liquid phase, mass transfer is rather intensified by the short diffusion path of the miniaturized channel than by flow deflection caused by the baffles. However, the miniaturized channel leads to a significantly higher pressure drop and a lower throughput than the enlarged channel with baffles. This could be inappropriate for processes in which the pressure drop represents the limiting factor.

The maximal possible allowed pressure drop represents a criterion to decide whether a miniaturized channel or a channel with baffles should be used. Furthermore, it is advantageous to use baffles in the liquid channel for processes which are dominated by the liquid-side mass transfer resistance. For processes determined by the gas-side mass transfer resistance, a miniaturized gas channel should be preferred, provided that the pressure drop in the gas channel is not a limiting factor.

Notation

Latin symbols

b = distribution coefficient
$[\mathbf{B}]$ = matrix defined by Eqs. 16 and 17, $m^2\ s^{-1}$
C = molar concentration, kmol m^{-3}
$\mathbf{C}$ = vector of molar concentrations, kmol m^{-3}
c = specific heat capacity, J $kg^{-1}\ K^{-1}$
d = diameter of a pipe, m
D = diffusion coefficient, $m^2\ s^{-1}$
$[\mathbf{D}] = [\mathbf{B}]^{-1}$ = diffusion matrix, $m^2\ s^{-1}$
g = gravitational acceleration, m s^{-2}
k = overall mass-transfer coefficient, m s^{-1}
$\vec{\mathbf{J}}$ = vector of diffusion fluxes, kmol $m^{-2}\ s^{-1}$
L = thickness of the membrane, m; length of a pipe, m
N = molar flux, kmol $m^{-2}\ s^{-1}$
$\vec{\mathrm{n}}$ = normal to the interface
p = pressure, Pa
q = heat flux, J $m^{-2}\ s^{-1}$
S = separation factor
t = time for diffusion defined by Eq. 32, s
T = temperature, K
u = velocity, m s^{-1}
$\vec{\mathrm{u}}$ = velocity vector, m s^{-1}
w = mass fraction
x = molar fraction in the liquid phase
$\bar{x}^2$ = square displacement, m^2
y = molar fraction in the gas phase
$\mathbf{y}$ = vector of molar fraction in the gas phase
z = cartesian coordinate

Greek letters

β = mass-transfer coefficient, m s^{-1}
γ = activity coefficient
δ = characteristic length for the mass transfer, m
ΔH^v = enthalpy of evaporation, J $kmol^{-1}$
ε = porosity of the membrane
η = dynamic viscosity, kg $m^{-1}\ s^{-1}$
λ = heat conduction coefficient, W $m^{-1}\ K^{-1}$
ρ = density, kg m^{-3}
τ = tortuosity

Subscripts and superscripts

0 = inlet
atm = atmospheric pressure
G = gas phase
i, j, k = component index
if = interface
L = liquid phase
M = membrane
SM = Stefan–Maxwell
tot = total

Dimensionless numbers

$Re = \frac{\rho u d}{\eta}$ = Reynolds number
$Sc = \frac{\eta}{\rho D_i}$ = Schmidt number

Literature Cited

1. Yue J, Chen G, Yuan Q, Luo L, Gonthier Y. Hydrodynamics and mass transfer characteristics in gas-liquid flow through a rectangular microchannel. *Chem Eng Sci*. 2007;62(7):2096–2108.
2. Cypes SH, Engstrom JR. Analysis of a toluene stripping process: a comparison between a microfabricated stripping column and a conventional packed tower. *Chem Eng J*. 2004;101(1–3):49–56.
3. Hibara A, Iwayama S, Matsuoka S, Ueno M, Kikutani Y, Tokeshi M, Kitamori T. Surface modification method of microchannels for gas-liquid two-phase flow in microchips. *Anal Chem*. 2005;77(3): 943–947.
4. Cai ZX, Fang Q, Chen HW, Fang ZL. A microfluidic chip based liquid-liquid extraction system with microporous membrane. *Anal Chim Acta*. 2006;556(1):151–156.
5. TeGrotenhuis WE, Cameron RJ, Butcher MG, Martin PM, Wegeng RS. Microchannel devices for efficient contacting of liquids in solvent extraction. *Sep Sci Technol*. 1999;34(6–7):951–974.
6. Aota A, Nonaka M, Hibara A, Kitamori T. Countercurrent laminar microflow for highly efficient solvent extraction. *Angew Chem Int Ed Engl*. 2007;46(6):878–880.
7. Seok DR, Hwang ST. Zero-gravity distillation utilizing the heat and pipe principle (micro-distillation). *AIChE J*. 1985;31(12):2059–2065.
8. Fanelli M, Arora R, Glass A, Litt R, Qui D, Silva L, Tonkovich AL, Weidert D. Micro-scale distillation: simualtion. *Comput Methods Multiphase Flow IV*. 2007;56:205–213.
9. Tonkovich AL, Jarosch K, Arora R, Silva L, Perry S, McDaniel J, Daly F, Littet B. Methanol production FPSO plant concept using multiple microchannel unit operations. *Chem Eng J*. 2008;135:S2–S8.
10. Sundberg A, Uusi-Kyyny P, Alopaeus V. Novel micro-distillation column for process development. *Chem Eng Res Des*. 2009;87(5A): 705–710.
11. Lam KF, Cao E, Sorensen E, Gavriilidis A. Development of multistage distillation in a microfluidic chip. *Lab Chip*. 2011;11(7):1311–1317.
12. Lam KF, Sorensen E, Gavriilidis A. Towards an understanding of the effects of operating conditions on separation by microfluidic distillation. *Chem Eng Sci*. 2011;66(10):2098–2106.
13. MacInnes JM, Ortiz-Osorio J, Jordan PJ, Priestman GH, Allen RWK. Experimental demonstration of rotating spiral microchannel distillation. *Chem Eng J*. 2010;159(1–3):159–169.
14. Tschernjaew J, Kenig EY, Górak A. Mikrodestillation von Mehrkomponentensystemen. *Chem Ingenieur Technik*. 1996;68(3):272–276.
15. Khayet M. Membranes and theoretical modeling of membrane distillation: A review. *Adv Colloid Interface Sci*. 2011;164(1–2):56–88.
16. Adiche C, Sundmacher K. Experimental investigation on a membrane distillation based micro-separator. *Chem Eng Process*. 2010; 49(4):425–434.
17. Garcia-Payo MC, Izquierdo-Gil MA, Fernandez-Pineda C. Wetting study of hydrophobic membranes via liquid entry pressure measurements with aqueous alcohol solutions. *J Colloid Interface Sci*. 2000; 230(2):420–431.
18. Rahimpour A, Madaeni SS, Mehdipour-Ataei S. Synthesis of a novel poly(amide-imide) (PAI) and preparation and characterization of PAI blended polyethersulfone (PES) membranes. *J Memb Sci*. 2008; 311(1–2):349–359.
19. Taylor R, Krishna R. *Multicomponent Mass Transfer*. Weinheim: Wiley, 1993.
20. Toor HL. Solution of the linearized equations of multicomponent mass transfer .1. *AIChE J*. 1964;10(4):448–455.
21. Comsol Multiphysics, 4.3 Model library of chemical engineering module in Comsol documentation, 2012.
22. Poling BE, Prausnitz JM, O'Connell JP. *The Properties of Gases and Liquids, 5th ed*. New Jork: McGraw-Hill, Co, 2001.
23. Gmehling V, Onken W, Arlt W. Vapour-liquid equilibrium data collection. Frankfurt/M.: Dechema Chemistry Data Series, 1977.
24. Mackley MR, Stonestreet P. Heat-tranfer and associated energy-dissipation for oscillatory flow in baffled tubes *Chem Eng Sci*. 1995; 50(14):2211–2224.

25. Dutta P, Dutta S. Effect of baffle size, perforation, and orientation on internal heat transfer enhancement. *Int J Heat Mass Transf*. 1998; 41(19):3005–3013.
26. Promvonge P, Sripattanapipat S, Tamna S, Kwankaomeng S, Thianpong C. Numerical investigation of laminar heat transfer in a square channel with 45 degrees inclined baffles. *Int Commun Heat Mass Transf*. 2010;37(2):170–177.
27. Olayiwola BO, Schaldach G, Walzel P. CFD study of effects of module geometry on forced convection in a channel with non-conducting fins and flow pulsation. *Chem Eng Technol*. 2010;33(10): 1706–1711.
28. Yang X, Yua H, Wang R, Fane AG. Analysis of the effect of turbulence promoters in hollow fiber membrane distillation modules by computational fluid dynamic (CFD) simulations. *J Memb Sci*. 2012; 415:758–769.
29. Phan AN, Harvey A. Development and evaluation of novel designs of continuous mesoscale oscillatory baffled reactors. *Chem Eng J*. 2010;159(1–3):212–219.
30. Ahmad AL, Lau KK, Abu Bakar MZ. Impact of different spacer filament geometries on concentration polarization control in narrow membrane channel. *J Memb Sci*. 2005;262(1–2):138–152.
31. Stroock AD, Dertinger SK, Ajdari A, Mezic I, Stone HA, Whitesides GM. Chaotic mixer for microchannels. *Science*. 2002; 295(5555):647–651.
32. Schonfeld F, Hardt S. Simulation of helical flows in microchannels. *AIChE J*. 2004;50(4):771–778.
33. Kim BS, Kwak BS, Shin S, Lee S, Kim KM, Jung HI, Cho HH. Optimization of microscale vortex generators in a microchannel using advanced response surface method. *Int J Heat Mass Transf*. 2011;54(1–3):118–125.
34. Chasanis P, Kehrmann KM, Kern J, Zecirovic R, Grünewald M, Kenig EY. Investigation of a microstructured high efficiency contactor. *Chem Eng Process*. 2011;50(11–12):1244–1251.
35. Mersmann A. Stoffübertragung. Berlin: Springer-Verlag, 1986.
36. Kärger J, Grinberg F, Heitjans P. *Diffusion Fundamentals*. Leipzig: Leipziger Universitätsverlag, 2005.
37. Srisurichan S, Jiraratananon R, Fane AG. Mass transfer mechanisms and transport resistances in direct contact membrane distillation process. *J Memb Sci*. 2006;277(1–2):186–194.

Appendix

The mass transport of methanol and water through a membrane pore is described above by Eqs. 22 and 23. These equations can be transformed to a simpler form. Equation 22 can be rearranged to

$$N^{G,if}_{methanol}(1-y_{methanol})=y_{methanol}N^{G,if}_{water} -C^{G}_{tot}\left(D_{11}\frac{dy_{methanol}}{dz}+D_{12}\frac{dy_{water}}{dz}\right) \tag{A1}$$

and Eq. 23 to

$$N^{G,if}_{water}(1-y_{water})=y_{water}N^{G,if}_{methanol} -C^{G}_{tot}\left(D_{21}\frac{dy_{methanol}}{dz}+D_{22}\frac{dy_{water}}{dz}\right) \tag{A2}$$

Inserting the expression for $N^{G,if}_{water}$ from Eq. A2 into Eq. A1 gives

$$N^{G,if}_{methanol}\left((1-y_{methanol})-\frac{y_{methanol}y_{water}}{(1-y_{water})}\right) =-\frac{y_{methanol}C^{G}_{tot}}{(1-y_{water})}\left(D_{21}\frac{dy_{methanol}}{dz}+D_{22}\frac{dy_{water}}{dz}\right) -C^{G}_{tot}\left(D_{11}\frac{dy_{methanol}}{dz}+D_{12}\frac{dy_{water}}{dz}\right) \tag{A3}$$

Introducing

$$T_1=(1-y_{methanol})-\frac{y_{water}y_{methanol}}{(1-y_{water})} \tag{A4}$$

and

$$T_2=-\frac{y_{methanol}}{(1-y_{water})} \tag{A5}$$

Equation A3 transforms to

$$N^{G,if}_{methanol}=\frac{T_2C^{G}_{tot}}{T_1}\left(D_{21}\frac{dy_{methanol}}{dz}+D_{22}\frac{dy_{water}}{dz}\right) -\frac{C^{G}_{tot}}{T_1}\left(D_{11}\frac{dy_{methanol}}{dz}+D_{12}\frac{dy_{water}}{dz}\right) \tag{A6}$$

In a similar way, inserting $N^{G,if}_{methanol}$ from Eq. A1 into Eq. A2, the following expression is obtained

$$N^{G,if}_{water}=\frac{T_4C^{G}_{tot}}{T_3}\left(D_{11}\frac{dy_{methanol}}{dz}+D_{12}\frac{dy_{water}}{dz}\right) -\frac{C^{G}_{tot}}{T_3}\left(D_{21}\frac{dy_{methanol}}{dz}+D_{22}\frac{dy_{water}}{dz}\right) \tag{A7}$$

where

$$T_3=(1-y_{water})-\frac{y_{water}y_{methanol}}{(1-y_{methanol})} \tag{A8}$$

and

$$T_4=-\frac{y_{water}}{(1-y_{methanol})} \tag{A9}$$

As the nitrogen concentration is considerably higher than that of methanol and water, the concentration change of N_2 along the membrane pore is negligible

$$\frac{dy_{N_2}}{dz}=0 \tag{A10}$$

Due to this assumption the derivative of methanol or water can be written as

$$\frac{dy_{methanol}}{dz}=\frac{d(1-y_{N_2}-y_{water})}{dz}=-\frac{dy_{water}}{dz} \tag{A11}$$

Using Eq. A11, Eqs. A6 and A7 can be transformed to

$$N^{G,if}_{methanol}=\frac{T_2C^{G}_{tot}}{T_1}\left(D_{21}\frac{dy_{methanol}}{dz}-D_{22}\frac{dy_{methanol}}{dz}\right) -\frac{C^{G}_{tot}}{T_1}\left(D_{11}\frac{dy_{methanol}}{dz}-D_{12}\frac{dy_{methanol}}{dz}\right) \tag{A12}$$

$$N^{G,if}_{water}=\frac{T_4C^{G}_{tot}}{T_3}\left(-D_{11}\frac{dy_{water}}{dz}+D_{12}\frac{dy_{water}}{dz}\right) -\frac{C^{G}_{tot}}{T_3}\left(-D_{21}\frac{dy_{water}}{dz}+D_{22}\frac{dy_{water}}{dz}\right) \tag{A13}$$

After integration over the pore length, one obtains

$$N^{G,if}_{methanol}=\frac{C^{G}_{tot}}{L_{membrane}\tau}\left((D_{21}-D_{22})\int_{y^{if}_{methanol}}^{y^{pore\ end}_{methanol}}\frac{T_2}{T_1}dy_{methanol}-(D_{11}-D_{12})\int_{y^{if}_{methanol}}^{y^{pore\ end}_{methanol}}\frac{1}{T_1}dy_{methanol}\right) \tag{A14}$$

$$N_{\text{water}}^{\text{G,if}} = \frac{C_{\text{tot}}^{\text{G}}}{L_{\text{membrane}}\tau}\left((-D_{11}+D_{12})\int_{y_{\text{water}}^{\text{if}}}^{y_{\text{water}}^{\text{pore end}}}\frac{T_4}{T_3}dy_{\text{water}}+(D_{21}-D_{22})\int_{y_{\text{water}}^{\text{if}}}^{y_{\text{water}}^{\text{pore end}}}\frac{1}{T_3}dy_{\text{water}}\right) \tag{A15}$$

The pore length is assumed to be equal to the membrane thickness L_{membrane} multiplied by the tortuosity τ which is determined by the correlation suggested in Ref. 37:

$$\tau = \frac{(2-\varepsilon)^2}{\varepsilon} \tag{A16}$$

The values of D_{ij} in Eqs. A14 and A15 are calculated as the arithmetic mean values based on the methanol and water concentrations at the pore inlet and outlet.

The integrals in Eqs. A14 and A15 were calculated numerically using the Simpson rule.

Manuscript received Aug. 28, 2014, and revision received Jan. 24, 2015.